Revisiting the dynamics of eyewall contraction of tropical cyclones

Yuanlong Li[1,2], Yuqing Wang[2,3*], and Yanluan Lin[1]

[1]Ministry of Education Key Laboratory for Earth System Modeling, Department of Earth System Science and Joint Center for Global Change Studies (JCGCS), Tsinghua University, Beijing, China

[2]International Pacific Research Center and Department of Atmospheric Sciences, School of Ocean and Earth Science and Technology, University of Hawaii at Manoa, Honolulu, Hawaii, USA

[3]State Key Laboratory of Severe Weather, Chinese Academy of Meteorological Sciences, China Meteorological Administration, Beijing, China

March 22, 2019 (submitted)
July 25, 2019 (revised)
Dateline

Submitted to ***The Journal of the Atmospheric Sciences***

[*]Corresponding author address:
Prof. Yuqing Wang
International Pacific Research Center
University of Hawaii at Manoa
404A/POST, 1680 East West Road,
Honolulu, HI 96822, USA.
Email: yuqing@hawaii.edu

Abstract

The dynamics of eyewall contraction of tropical cyclones (TCs) has been revisited in this study based on both three-dimensional and axisymmetric simulations and dynamical diagnostics. Because the eyewall contraction is closely related to the contraction of the radius of maximum wind (RMW), its dynamics is thus often studied by examining the RMW tendency in previous studies. Recently, Kieu and Stern et al., respectively, proposed two different frameworks to diagnose the RMW tendency, but had different conclusions. In this study, the two frameworks are evaluated first based on theoretical analysis and idealized numerical simulations. It is shown that the framework of Kieu is a special case of the earlier framework of Willoughby et al. if the directional derivative is applied. An extension of Stern et al.'s approach can not only reproduce but also predict the RMW tendency. A budget of the azimuthal mean tangential wind tendency indicates that the contributions by radial and vertical advections to the RMW tendency vary with height. Namely, radial advection dominates the RMW contraction in the lower boundary layer and vertical advection favors the RMW contraction in the upper boundary layer and lower troposphere. In addition to the curvature, the increase of radial gradient of horizontal mixing (including the resolved eddy mixing in three-dimensions) near the eyewall prohibits the eyewall contraction in the lower boundary layer. Besides, the vertical mixing including surface friction also plays an important role in the cessation of eyewall contraction in the lower boundary layer.

1. Introduction

The eyewall contraction is closely related to intensification, often rapid intensification, of a tropical cyclone (TC). Therefore, understanding the dynamics of eyewall contraction is of fundamental importance for understanding the dynamics of TC intensification. However, although the eyewall contraction is a common feature during the TC intensification, its dynamics has not been well understood so far. Because the eyewall contraction is closely tied with the contraction of the radius of maximum wind (RMW), the dynamics of eyewall contraction is thus often studied by examining the change of the RMW in previous studies (Willoughby et al. 1982, hereafter W82; Kieu 2012, hereafter K12; Stern et al. 2015, hereafter S15). Note that although the inner core of a TC could be quite asymmetric and the RMW may vary azimuthally, the RMW is often defined using the azimuthal mean tangential wind, which may change with height (S15).

Although no theory exists for the size of the RMW or its change, previous studies have attempted to examine key processes to the size of the RMW based on idealized high-resolution numerical simulations (e.g., Xu and Wang 2010a, b). Wang and Xu (2010) and Xu and Wang (2010a) showed that the RMW would contract more if the surface enthalpy flux outside 2~2.5 times of the RMW was removed. This is because the removal of surface enthalpy flux in the outer region suppressed outer rainband activities and thus diabatic heating outside the eyewall, which otherwise would reduce low-level inflow into the eyewall and reduce the eyewall contraction (cf. Xu and Wang 2010a). Xu and Wang (2010b) found that both the initial size of the RMW and the initial moisture in the lower troposphere could affect the rainband activities and thus the quasi-steady

RMW of a simulated TC. They also proposed that the effects of the initial vortex size and initial moisture are coupled with each other, although the quasi-steady RMW is more sensitive to the initial vortex size. Rotunno and Bryan (2012) found that the steady-state RMW is insensitive to the vertical mixing length, but sensitive to the horizontal mixing length in their simulations using an axisymmetric TC model, while Bu et al. (2017) showed that the RMW tends to be larger with stronger vertical mixing in the boundary layer or higher sea surface temperature. Bu et al. (2017) also found that cloud-radiative forcing can increase the RMW because the cloud-radiative forcing can promote rainband activities.

Note that the mechanisms for the steady-state RMW in the mature phase and the RMW contraction during the intensification stage could be different. For example, a larger surface drag coefficient (C_D) usually results in a faster contraction rate (e.g., Bryan 2013; Smith et al. 2014), but there was no obvious relationship between C_D and the steady-state RMW (e.g., Bryan 2012, 2013) unless C_D was rather small or zero (Kilroy et al. 2017). Similar to the steady-state RMW, the contraction rate of RMW has been shown to be also sensitive to many parameters in previous numerical studies. For instance, a faster contraction rate can occur in simulations with a smaller Coriolis parameter (Smith et al. 2015; Deng et al. 2018). These are only some qualitative results from numerical simulations since the contraction rate of the RMW has not been the main focus of these studies.

Shapiro and Willoughby (1982) proposed a mechanism to explain the contraction of RMW in a TC based on balanced vortex dynamics. They showed that the tangential wind tendency in response to diabatic heating in the eyewall is greater inside of the RMW than at the RMW, leading to not only the intensification of a TC vortex but also the contraction of the RMW. This has become the major dynamical mechanism used for the explanation of the contraction of the RMW or the eyewall of a TC. However, this conceptual explanation could not be used to quantitatively estimate the contraction of the RMW. W82 proposed a kinematic RMW contraction equation following a moving frame of reference of the RMW, which showed good agreements with observations for the hurricane cases diagnosed.

Some recent efforts have been devoted to quantitatively estimate the contraction rate of RMW (K12; S15). K12 derived an equation for the contraction rate of RMW based on the tangential wind equation and a kinematic equation of the RMW under some assumptions/approximations (see Section 2c). K12 proposed a dependence of the contraction rate of RMW on both the radial inflow and surface friction, with the former favoring the inward penetration of angular momentum and thus the RMW contraction and the latter being responsible for the slowdown and termination of the contraction. S15 proposed a method to diagnose the contraction rate of RMW based on the geometrical definition of the RMW, which was attributed to the radial gradient of tangential wind tendency and the curvature (or sharpness) of radial profile of tangential wind at the RMW. Kieu and Zhang (2017) presented concerns with the work of S15 in terms of the lack of dynamics to the contraction rate of the RMW because the method was based purely on kinematics. S15 and Stern et al. (2017) also argued that the equation of K12 could not explain the contraction rate of RMW because of some contradictory mathematical assumptions used in the derivation of the equation (see Section 2c). All of the concerns in S15 and Stern et al. (2017) for K12 were disputed by Kieu and Zhang (2017).

In this study, the dynamics of the RMW contraction is revisited based on both theoretical consideration and diagnostics of numerical simulations. We first review the existing theories and compare their contraction rates of RMW with those from idealized numerical simulations. Both axisymmetric and three-dimensional simulations are conducted to understand the dynamics of the eyewall contraction. The rest of paper is organized as follows. Section 2 briefly reviews the main existing theories on eyewall contraction, including the balanced dynamics and those discussed in W82, K12, and S15. An evaluation of W82 and S15 using results from idealized simulations and an azimuthal mean tangential wind budget is discussed in Section 3, in which a three-dimensional, cloud-permitting high-resolution model is used. The axisymmetric dynamics of the RMW contraction and the roles of horizontal and vertical mixings are discussed in Section 4 using a series of axisymmetric simulations. Concluding remarks are given in Section 5.

2. A brief review of existing theories

a. Balanced vortex dynamics

Balanced vortex dynamics assumes a quasi-balanced basic axisymmetric vortex that is in both hydrostatic and gradient wind balances. Given the spatial distributions of heat source and momentum forcing, a partial differential equation for the streamfunction of the transverse circulation, namely, the so-called Sawyer-Eliassen equation (SEQ, Eliassen 1951) can be obtained.

Since the SEQ is a linear partial differential equation and its solutions to different forcings are additive and thus can be used to understand the response of the transverse circulation in a TC vortex to various heat sources or momentum forcing. Because the low-level inflow in the transverse circulation can bring absolute angular momentum inward to spin up the tangential wind, the solution of the SEQ has been used to understand the TC intensification and the eyewall contraction (e.g., Shapiro and Willoughby 1982; Schubert and Hack 1982; Pendergrass and Willoughby 2009; Bui et al. 2009; Heng and Wang 2016; Heng et al. 2017), the TC outer-core size change (e.g., Fudeyasu and Wang 2011), and the secondary eyewall formation (e.g., Zhu and Zhu 2014; Wang et al. 2016).

Shapiro and Willoughby (1982) found that the low-level tangential wind tendency in response to diabatic heating in the eyewall is greater inside of the RMW than at the RMW. As a result, as the TC vortex intensifies, its RMW would move inward, namely experiencing a contraction. The simultaneous intensification and eyewall contraction have been observed in real TCs (e.g., W82; Willoughby 1990) and in numerical simulations (e.g., Bryan 2013; Smith et al. 2014; Smith et al. 2015, Wang and Heng 2016; Deng et al. 2018). However, recent observations (e.g., Wang and Wang 2013; Stern et al. 2015; Qin et al. 2016) indicate that it is very common for the asynchrony between TC intensification and eyewall contraction. This means that although the balanced vortex dynamics has been considered as a dominant dynamical mechanism responsible for the contraction of RMW or the eyewall of a TC, it could not explain all aspects of the eyewall contraction. Furthermore, it only provides a qualitative explanation but not a quantitative estimation of the RMW contraction.

b. Willoughby et al. (1982)

As reviewed by Kieu and Zhang (2017), W82 proposed an RMW contraction equation, which can be derived from the definition of the directional derivative in a moving frame of reference following the RMW of a TC, namely

$$\left(\frac{d\bar{V}}{dt}\right)_{\mathrm{RMW}} = \left(\frac{\partial\bar{V}}{\partial t}\right)_{rmw} + \frac{d\mathrm{RMW}}{dt}\left(\frac{\partial\bar{V}}{\partial r}\right)_{\mathrm{RMW}}, \quad (1)$$

where *r* is the radial distance from the TC center; overbar denotes azimuthal mean or the variable in an axisymmetric framework as in W82. Note that the subscript "*rmw*" denotes the arriving radial location of the RMW. Equation (1) indicates that the change in tangential wind $\bar{V}$ following the RMW, namely the intensity change, is caused by the local change of tangential wind at the arriving radial location of the RMW (first term on the rhs) and the advective change of tangential wind due to the contraction of the RMW (second term on the rhs). W82 also assumed that the local change of tangential wind at the arriving RMW is primarily determined by the maximum local tangential wind tendency. Equation (1) can then be rearranged as follows

$$\frac{d\mathrm{RMW}}{dt} = \frac{\left(\frac{d\bar{V}}{dt}\right)_{\mathrm{RMW}} - \left(\frac{\partial\bar{V}}{\partial t}\right)_{rmw}}{(\partial\bar{V}/\partial r)_{\mathrm{RMW}}}. \quad (2)$$

In Eq. (2), $(d\bar{V}/dt)_{\mathrm{RMW}}$ is the intensification rate of the storm; $(\partial\bar{V}/\partial t)_{rmw}$ denotes local tangential wind tendency at the arriving radius of the RMW. Note that although the radial gradient of tangential wind, $\partial\bar{v}/\partial r$, should be zero at the RMW by definition, here $(\partial\bar{V}/\partial r)_{\mathrm{RMW}}$ should be considered being related to the upwind radial gradient of tangential wind, i.e., relative to the arrival location of the RMW (noted as subscript "rmw"). This means that $(\partial\bar{V}/\partial r)_{\mathrm{RMW}}$ should be calculated using an upwind (backward in this case) finite-differencing scheme, as used in W82 and recently emphasized by Kieu and Zhang (2017, see their Fig. 1). In practical applications of W82, the radial gradient of tangential wind inside the current RMW was approximated as $\bar{V}_{max}/\mathrm{RMW}$, namely a Rankine vortex wind profile was assumed inside the RMW. Note that because the local tendency of tangential wind at the arriving RMW needs to be known before the tendency of RMW can be calculated, Eq. (2) can only be used for diagnostic purpose and could not be used to predict the contraction of RMW. Furthermore, Eq. (2) is a pure kinematic contraction rate and does not provide understanding of dynamics of the RMW contraction. To distinguish the notions of "dynamics" and "kinematics/geometrics", one must recall the difference between "physics" and "mathematics". The "dynamical" process reveals the physical reasoning for RMW contraction and can thus provide understanding of physical mechanisms, while the "kinematics/geometrics" mathematically describes the contraction rate of RMW with little insights into dynamics of RMW contraction. For example, in the kinematic case of W82, the tangential wind profiles at both the current and arriving RMW should be given in order to know the RMW change.

c. Kieu (2012)

K12 and Kieu and Zhang (2017) developed an equation for the contraction rate of the RMW of a TC. They started with the tangential wind equation at the RMW for an axisymmetric TC vortex given below

$$\frac{\partial \bar{V}}{\partial t} = -\bar{U}\frac{\partial \bar{V}}{\partial r} - \frac{\bar{U}\bar{V}}{\text{RMW}} - \bar{W}\frac{\partial \bar{V}}{\partial z} - f\bar{U} + \bar{F_\lambda}^*, \quad (3)$$

where z and f denote height and Coriolis parameter; the uppercases and the superscript * denote those variables at the RMW exactly; U and W denote radial and vertical velocity at the RMW; and, $\bar{F_\lambda}^*$ is the momentum forcing, including subgrid horizontal and vertical turbulent mixing (and surface friction), and eddy advection if the asymmetric effect is included, at the RMW. By assuming (i) wind profile within and at the RMW is a Rankine vortex, i.e., $\bar{v}(t,r) \sim \bar{\Omega}(t)r$, and, (ii) the angular velocity, $\bar{\Omega}$, is a strict function of time within and at the RMW, i.e., $\partial\bar{\Omega}(\mathrm{t})/\partial t = d\bar{\Omega}(\mathrm{t})/dt$, and further considering $\partial\bar{V}(t, \text{RMW})/\partial r = 0$, Eq. (3) can be rewritten as

$$\frac{d\bar{\Omega}^*}{dt}\text{RMW} = -\bar{U}\bar{\Omega}^* - \bar{W}\frac{\partial \bar{V}}{\partial z} - f\bar{U} + \bar{F_\lambda}^*. \quad (4)$$

K12 also assumed that the wind profile within the RMW maintained as a Rankine vortex at all times, implying $\bar{V}(t) = \bar{\Omega}^*(\mathrm{t}) \times \text{RMW}(t)$, thus one can have

$$(\frac{d\bar{V}}{dt})_{\text{RMW}} = \frac{d\bar{\Omega}^*}{dt}\text{RMW} + \frac{d\text{RMW}}{dt}\bar{\Omega}^*, \quad (5)$$

where $(\,)_{\text{RMW}}$ denotes an operator, in which the derivation follows the RMW rather than the air parcel. By definition, the $(d\bar{V}/dt)_{\text{RMW}}$ is the intensification rate of the TC. Plugging Eq. (5) into Eq. (4), one can get

$$\frac{d\text{RMW}}{dt}\bar{\Omega}^* = (\frac{d\bar{V}}{dt})_{\text{RMW}} + \bar{U}(\bar{\Omega}^* + f) + \bar{W}\frac{\partial \bar{V}}{\partial z} - \bar{F_\lambda}^*. \quad (6)$$

Note that Eq. (6) would be reduced to Eq. (6) in K12 if $\partial\bar{V}/\partial z$ is omitted and $\bar{F_\lambda}^*$ is assumed for a slab boundary layer in an axisymmetric TC vortex. Equation (6) can be rewritten as

$$\frac{d\mathrm{RMW}}{dt} = \frac{\mathrm{RMW}}{\bar{V}}\left(\frac{d\bar{V}}{dt}\right)_{\mathrm{RMW}} + \frac{\mathrm{RMW}}{\bar{V}}\bar{U}(\bar{\Omega}^{*} + f) + \frac{\mathrm{RMW}}{\bar{V}}\bar{W}\frac{\partial\bar{V}}{\partial z} - \frac{\mathrm{RMW}}{\bar{V}}\bar{F}_{\lambda}^{\ *}. \qquad (7)$$

The four terms on the rhs of Eq. (7) denote the TC intensification forcing, inflow effect, vertical advection effect, and subgrid vertical turbulent mixing including surface friction and eddy advection, respectively. According to K12, Kieu and Zhang (2017), and Qin et al. (2018), in the boundary layer, the intensification forcing and vertical advection effect are negligible compared to the inflow effect and the frictional effect. In addition, the inflow term can be simplified as $\bar{U}$, because $\bar{\Omega}^{*} \gg f$. That is, the boundary layer inflow advects angular momentum inward and thus contributes to the RMW contraction and surface friction slows down or retards the RMW contraction.

The framework of K12 and Kieu and Zhang (2017) outlined above was challenged by S15 and Stern et al. (2017). First, S15 indicated that the total derivative of $\bar{\Omega}^{*}$, $(d\bar{\Omega}^{*}/dt)$ is not equal to its partial derivative $(\partial\bar{\Omega}^{*}/\partial t)$, because $\bar{\Omega}^{*}$ should be also a function of r, but this argument seems to be inconsistent with the assumption of K12 or in Kieu and Zhang (2017) as mentioned above. In addition, Stern et al. (2017) noted that the contraction rate in the simulations of K12 obviously increased with surface friction or C_D, which is in contradictory to the explanation of Eq. (6). The positive correlation between C_D and the eyewall contraction rate has been also reported in previous studies (e.g., Bryan 2013; Smith et al. 2014; Heng and Wang 2016). We also noticed that the dependence of RMW contraction rate on C_D should be a local behavior, that is, in addition to surface friction, the radial advection in Eq. (7) and the TC structure during the initial spin-up period will also change considerably if C_D is changed (e.g., Smith et al. 2014; Heng et al. 2016).

Therefore, it is hard to tell the role of surface friction in the RMW contraction just by changing C_D from the beginning of a simulation.

Here, we would show that Eq. (7) can be considered as a special case of W82. Based on Eq. (3) the sum of the last three terms on the rhs of Eq. (6) is exactly the negative local tendency of the azimuthal mean tangential wind at the RMW because $\partial\bar{V}/\partial r = 0$, i.e., $(\partial V/\partial t)_{\mathrm{RMW}} = -\bar{U}(\bar{\Omega}^* + f) - \bar{W}\,\partial\bar{V}/\partial z + \bar{F}_\lambda{}^*$. Plugging this into Eq. (7) yields

$$\frac{d\mathrm{RMW}}{dt} = \frac{\mathrm{RMW}}{\bar{V}}\left[\left(\frac{d\bar{V}}{dt}\right)_{\mathrm{RMW}} - \left(\frac{\partial\bar{V}}{\partial t}\right)_{\mathrm{RMW}}\right] \quad (8)$$

The first term is related to the intensification rate of the TC, $(d\bar{V}/dt)_{\mathrm{RMW}}$, and the second term is related to the local change of tangential wind at the RMW, $(\partial\bar{V}/\partial t)_{\mathrm{RMW}}$. Note that Eq. (8) looks similar to Eq. (2) if one assumes that the tangential wind within and at the RMW strictly satisfies a Rankine vortex, i.e., $\partial\bar{v}/\partial r\,|_{r\leq\mathrm{RMW}} = \bar{V}/\mathrm{RMW}$, which is the key assumption of K12 and also an assumption used in estimating the RMW contraction based on the flight-level data in W82. The major difference between Eq. (8) and Eq. (2) lies in where the local tendency of the azimuthal mean tangential wind is defined. In Eq. (2) it is defined at the arriving point of the RMW, while in Eq. (8) it seems to be defined at the current time. Since the contraction of RMW could not be evaluated if the local change of tangential wind is defined at the current time (see Fig. 1 of Kieu and Zhang 2017), this suggests an alternative problem of K12. As a result, only when the local tendency of tangential wind or the last three terms are evaluated at the arriving point of the RMW, Eq. (7) can be used to diagnose the contraction rate of the RMW. However, in this case, Eq. (7) becomes equivalent to Eq. (2) and it does not provide any extra dynamical insights into the contraction of the RMW as claimed by K12 and Kieu and Zhang (2017). Therefore, K12 will not be included in the following discussion.

d. Stern et al. (2015)

Based on the kinematic/geometric definition of the RMW (i.e., $\partial\bar{V}(r,t)/\partial r\,|_{r=\mathrm{RMW}} = 0$), a diagnostic equation for the contraction rate of the RMW can be derived without any assumption as given in S15, i.e.,

$$\frac{d\mathrm{RMW}}{dt} = -\frac{(\partial/\partial r)(\partial\bar{V}/\partial t)}{\partial^2\bar{V}/\partial r^2}\Big|_{\mathrm{RMW}}. \tag{9}$$

The numerator and denominator of Eq. (9) denote the radial gradient of local time tendency of the azimuthal mean tangential wind and the curvature of the azimuthal mean tangential wind in the radial direction at the RMW, respectively. Because of the radially peaked tangential wind profile at the RMW, the curvature is always negative. Two main implications can be inferred from Eq. (9). First, for a given radial gradient of tangential wind tendency at the RMW, the TC with a stronger curvature or sharpness at the RMW is harder to contract. The curvature, however, is usually become sharper with the intensification of a TC, which was hypothesized as the reason for the cessation of the RMW contraction in S15. Second, because the curvature is negative definite at the RMW, the sign of the RMW tendency depends on the radial gradient of tangential wind tendency at the RMW, i.e., the RMW tends to contract if $\partial(\partial\bar{V}/\partial t)/\partial r < 0$ and vice versa. However, these were regarded as an invalid statement by Kieu and Zhang (2017), who argued that there was no involved dynamics of the RMW contraction because the radial gradient of tangential wind tendency is not dynamically determined in S15. Although later Stern et al. (2017) pointed out that it was possible to substitute the tangential wind tendency equation into Eq. (9) as shown in their Eq. (24), and as applied in Tang et al. (2019) for explaining the different RMW contraction rates under different radiative forcings, they did not provide any detailed insight into the dynamical processes that control the contraction of the RMW.

3. Evaluation of W82 and S15

In this section, the performances of W82 and S15 in capturing the contraction rate of the RMW are evaluated using the outputs from three-dimensional high-resolution idealized numerical simulations and a tangential wind budget analysis.

a. Model and experimental design

The Weather Research and Forecasting (WRF) model version 3.8.1 (Skamarock et al. 2008) was used, which is a fully compressible, nonhydrostatic model with a terrain-following vertical coordinate. The triply nested and fixed domains were used with the finest resolution of 2 km in the innermost domain. Physical parameterizations used in our simulations include the Mellor-Yamada Nakanishi Niino (MYNN) Level 2.5 scheme (Nakanishi and Niino 2009) for the surface layer and the planetary boundary layer processes, the Dudhia shortwave radiation scheme (Dudhia 1989), the Rapid Radiative Transfer Model (RRTM; Mlawer et al. 1997) for longwave radiation scheme, the Thompson microphysical scheme (Thompson et al. 2008) for cloud microphysics, and the Kain–

Fritsch cumulus parameterization (Kain 2004) in the outermost 18-km mesh only. The average moist tropical sounding during June-October 2002 of Dunion and Marron (2008) was used as the unperturbed environment with the sea surface temperature was fixed at 29°C.

Two idealized three-dimensional simulations were conducted. In the control experiment, the experimental design followed that in Zhu and Zhu (2014), in which a strong initial TC vortex with the maximum tangential wind speed of 36 m s^{-1} at a radius of 45 km was used. A sensitivity experiment was conducted to ensure the robustness of the results from the control experiment. The sensitivity experiment was the same as the control experiment except that a weaker initial TC vortex with the maximum tangential wind speed of 18 m s^{-1} was used. All results discussed below were based on the model outputs from the innermost domain at 10-min intervals.

To make the finite differencing smoother enough to facilitate the evaluation of the theoretical work summarized in section 2, similar to S15, we first filtered out the small-scale perturbations less than 40 min in time using a time mean and less than 8 km in radial direction using a spatial average, and then we interpolated all the azimuthal mean variables from a radial grid spacing of 2 km into a 50-m grid spacing using the cubic spline interpolation. The results discussed below are all based on the filtered variables and the results are not sensitive to the filtering scale qualitatively.

b. Evaluation results

Consistent with previous studies, in the control experiment, after about 15 h initial adjustment, a rapid contraction of the RMW occurred, which stopped well before the end of intensification (Fig.

1). The largest hourly contraction rate reached ~16 km h^{-1} at about 17 h of the simulation. The RMW remained almost constant after about 22.5 h, but the TC continued to intensify. This means that the contraction of RMW is not necessarily accompanied by TC intensification, which is consistent with observations (Stern et al. 2015; Qin et al. 2016; Wang and Wang 2013). Figure 2a compares the time tendency of the RMW from the control experiment with those calculated using Eqs. (2) and (9), respectively, from W82 and S15 at a height of 250 m, which is the same as in S15. Note that here the finite-differencing scheme for W82 exactly followed that suggested by Kieu and Zhang (2017) using the tangential wind profile at the arriving RMW, and a centered finite-difference scheme was used for S15 in both time and space at the current time and current location of RMW. We can see that the diagnosed tendency of the RMW using Eq. (2) or Eq. (9) is almost identical to that of the model simulation. This is not surprising since both equations were derived without any mathematical simplification, although Eqs. (2) and (9) are not equivalent mathematically (Kieu and Zhang 2017). In addition, there is almost no error for W82 (Fig. 2c) because it is a fully closed kinematic model, in which the arriving profile has been provided, as mentioned earlier. As we can see from Figs. 2b and 2d, the conclusion is unchanged with an initially weaker TC vortex.

To understand contributions to the RMW contraction in S15, we show in Fig. 3a the time series of both the radial gradient of the azimuthal mean tangential wind tendency and the curvature of the azimuthal mean tangential wind in the radial direction at the RMW and 250-m height. We can see from Fig. 3a that the curvature of tangential wind was negative definite throughout the simulation as mentioned earlier, while the radial gradient of tangential wind tendency showed large variability with both negative and positive values corresponding to the contraction and expansion of RMW in the simulation (Fig. 2). During the early stage of the rapid RMW contraction period 15–19 h (Fig. 1), the radial gradient of the azimuthal mean tangential wind tendency at the RMW was largely negative and the curvature of the azimuthal mean tangential wind was small, corresponding to the rapid contraction of the RMW. With the rapid contraction, the curvature of the azimuthal mean tangential wind increased rapidly, and the tangential wind showed large sharpness near the RMW (Fig. 3b). S15 attributed the cessation of the RMW contraction to the increase in the curvature or sharpness of tangential wind. In our simulation, both the decrease in the negative radial gradient of azimuthal mean tangential wind tendency and the increase in the sharpness of the azimuthal mean tangential wind contributed to the cessation of the RMW contraction as we can see from Figs. 2 and 3a.

c. The azimuthal mean tangential wind budget

Based on the above analysis, the method in S15 can be used as a good starting point to understand the dynamical processes responsible for the RMW contraction (or the RMW change, in general). Because of the negative definite nature of $\partial^2\bar{V}/\partial r^2$ in Eq. (9), the sign of the RMW tendency depends on the radial gradient of the azimuthal mean tangential wind tendency at the RMW $(\partial/\partial r)(\partial\bar{V}/\partial t)$. To understand dynamical processes that contribute to the radial gradient of the azimuthal mean tangential wind in Eq. (9), we performed a budget analysis for the azimuthal mean tangential wind tendency as in Fudeyasu and Wang (2011) and Qin et al. (2018). The budget equation can be given as,

$$\frac{\partial \bar{v}}{\partial t} = -\bar{u}\bar{\zeta}_a - \bar{w}\frac{\partial \bar{v}}{\partial z} - \overline{u'\zeta_a{}'} - \overline{w'\left(\frac{\partial v'}{\partial z}\right)} - \overline{\frac{\alpha'}{r}\left(\frac{\partial p'}{\partial \lambda}\right)} + \bar{F}_{fric} + \bar{F}_{diff}, \tag{10}$$

where variables or terms with overbar denote the azimuthal mean, and those with prime denote the deviations from the corresponding azimuthal mean, $\varsigma_a = \partial v/\partial r + v/r + f$ is the absolute vertical vorticity, p is air pressure, λ is the azimuth, and α is the specific volume of dry air. The first two terms on the rhs of Eq. (10) denote the mean horizontal (radial) advection (ADV_H) and mean vertical advection (ADV_V); followed by eddy horizontal advection (Eddy_H), eddy vertical advection (Eddy_V), perturbation pressure gradient force, turbulent vertical mixing including surface friction (Ff), and subgrid-scale horizontal diffusion (Diff), respectively. Note that our results show that the perturbation pressure gradient force is rather small, at least four orders smaller in magnitude than the leading terms in Eq. (10), and thus is omitted in the following discussions. Note also that the RMW tilts mostly outward with height after the initial adjustment. This implies the importance of boundary layer dynamics for the contraction of RMW. Therefore, the budget analysis is confined below 3 km.

To ensure a nearly residual-free budget analysis, in addition to the instantaneous values, all the 10-min mean $\bar{u}$, $\bar{v}$, $\bar{w}$, horizontal advection, vertical advection, turbulent vertical mixing (including surface friction), subgrid-scale horizontal diffusion, and pressure gradient force were directly calculated during the model integration. All these variables were then interpolated into the cylindrical coordinates. The TC center was defined as the circulation center, which maximizes the

TC maximum tangential wind speed at 250 m height above the sea surface. Note that during the WRF integration only the total advections ($-\overline{u\zeta_a}$ and $-\overline{w\,\partial v/\partial z}$) could be explicitly given and saved. This means that both the eddy advection terms ($-\overline{u'\zeta_a{}'}$ and $-\overline{w'(\partial v'/\partial z)}$) and the mean advections ($-\bar{u}\overline{\zeta_a}$ and $-\bar{w}\,\overline{\partial v/\partial z}$) should be calculated off-line. However, the off-line calculations would induce some numerical errors in the partitioned mean and eddy advections due to the coordinate transformation, interpolation, and the use of different finite-differencing schemes. To reduce any bias in such partitioning, we first directly calculated both mean and eddy advections off-line and then indirectly obtained the mean (eddy) advection terms by subtracting the off-line directly calculated eddy (mean) advections from the WRF-output total advections. Finally, the mean (eddy) advections used in the final budget analysis are defined as the average of the two mean (eddy) advections obtained above. In this way, the calculation errors are distributed equally between the mean and eddy advections. Note that to minimize errors that might be introduced due to the use of different finite-differencing algorithms in calculating the advection terms in the WRF model and in the budget, as in the WRF model, the staggered grid finite-differencing in both vertical and radial directions was used to improve the precision. Figure 4 compares the eddy advection terms obtained from the above method and that directly calculated using the 10-min mean wind field at 19 h (Figs. 4a–d) and 21 h (Figs. 4e–h). The overall patterns are very similar except some discrepancies. Note that the 10-min mean field was used to define the storm center to avoid any inconsistencies in the calculated eddy contributions. This might introduce some extra errors. However, because the TC motion in 10 minutes in the simulation on an *f*-plane in a quiescent environment is often less than one half of the finest grid spacing (often less than 1 km), the errors would not affect our main conclusions. Therefore, the budget results can be used to understand contributions of various forcing processes to the RMW contraction.

To provide a general view on the structure of the local azimuthal mean tangential wind tendency and their relative position to the RMW, a 40-min averaged budget during the rapid RMW contraction period (19 h) is shown in Fig. 5. Note that the azimuthal mean tangential wind tendencies from both the model and budget are shown in Fig. 5 for a comparison. Clearly, the budget reproduced the tendency structure from the simulation very well (Figs. 5a, b), with negligible errors (~10^{-5} m s^{-1} h^{-1}) from interpolations. As we can see from Fig. 5, the tangential wind tendency inside the RMW is larger than that outside, which results in the contraction of the RMW during this period (cf. Figs. 1 and 2a). Some key points can be noticed by comparing all individual terms in Figs. 5c–5h. First, the contribution by mean advection varies with height. For example, the mean vertical advection (ADV_V) contributes to an expansion below ~300 m but a contraction above; the mean horizontal advection (ADV_H) contributes to a contraction of the RMW below ~400 m but an expansion above. The turbulent vertical mixing including surface friction (Ff), eddy horizontal advection (Eddy_H), and subgrid-scale horizontal diffusion (Diff) all contribute to the RMW expansion in the boundary layer, and eddy vertical advection (Eddy_V) contributes to the RMW contraction at this time.

Following Stern et al. (2017), substituting Eq. (10) into Eq. (9) and omitting the perturbation pressure gradient force, we get

$$\frac{d\mathrm{RMW}}{dt} = \left[\frac{\frac{\partial}{\partial r}(\bar{U}\bar{\zeta}_a)}{\partial^2\bar{V}/\partial r^2} + \frac{\frac{\partial}{\partial r}(\bar{W}\frac{\partial\bar{V}}{\partial z})}{\partial^2\bar{V}/\partial r^2} + \frac{\frac{\partial}{\partial r}(\overline{u'\zeta_a'})}{\partial^2\bar{V}/\partial r^2} + \frac{\frac{\partial}{\partial r}(\overline{w'\left(\frac{\partial v'}{\partial z}\right)})}{\partial^2\bar{V}/\partial r^2} - \frac{\frac{\partial}{\partial r}(\bar{F}_{fric})}{\partial^2\bar{V}/\partial r^2} - \frac{\frac{\partial}{\partial r}(\bar{F}_{diff})}{\partial^2\bar{V}/\partial r^2}\right]\Big|_{\mathrm{RMW}}. \quad (11)$$

Considering the contribution by mean advection to the RMW tendency varies with height (cf. Figs. 5c, d), and the turbulent vertical mixing is large below 500-m height (cf. Fig. 5e), two different integral averages are calculated, i.e., between 0–500 m (the lower boundary layer) and between 500–1500 m (the upper boundary layer and lower troposphere), to illustrate the contribution of each tangential wind tendency forcing to the RMW tendency. Figure 6 shows each integral-averaged tangential wind tendency at the RMW [Figs. 6a and 6b; cf. Eq. (10)] and the corresponding contribution to the RMW tendency [denoted by the prefix "S15" in Figs. 6c and 6d; cf. Eq. (11)].

In the lower boundary layer, as expected, the mean horizontal advective forcing (S15_ADV_H) dominates the contraction of the RMW (Fig. 6c), consistent with its large magnitude (ADV_H, Fig. 6a). The subgrid-scale horizontal diffusion forcing (S15_Diff) and eddy vertical advective forcing (S15_Eddy_V) contribute marginally to the RMW contraction (Fig. 6c), consistent with their small magnitudes (Fig. 6a). In addition, although the mean vertical advection (ADV_V) at the RMW is much larger than the eddy vertical advection (Eddy_V) (Fig. 6a), its contribution to the RMW tendency is small and comparable with S15_Eddy_V (Fig. 6c). The role of mean vertical advection in the RMW tendency (S15_ADV_V) is alternately positive and negative during the simulation (Fig. 6c). Consistent with K12, the turbulent vertical mixing including surface friction (Ff) contributes to the RMW expansion (Fig. 6c). Besides, the increase of eddy horizontal advective forcing (S15_Eddy_H) also plays an important role in the cessation of RMW contraction from the later rapid contraction stage (after ~20 h) (Fig. 6c). Note that although Ff in the later rapid contraction stage is comparable with Eddy_H (Fig. 6a), its contribution (S15_Ff) to the RMW tendency is smaller than S15_Eddy_H (Fig. 6c). This difference is understandable, because $\bar{F}^{*}_{fric} \sim -C_D/H\,[\bar{V}\sqrt{(\bar{V}^2+\bar{U}^2)}] \sim -C_D\bar{V}^2/H$ (see K12), considering $\bar{V}^2 \gg \bar{U}^2$ therefore, $\partial\bar{F}^{*}_{fric}/\partial r \sim -(2\,C_D\bar{V}/H)(\partial\bar{V}/\partial r) \sim 0$, if we assume C_D and H are constant. Indeed, the contours of Ff near the RMW are almost perpendicular to the RMW (Fig. 5e), indicating a small radial gradient of Ff at the RMW, except for those levels near the surface where the approximation, $\bar{V}^2 \gg \bar{U}^2$ is often invalid. However, the contours of Eddy_H near the RMW in the lower boundary layer are almost parallel to the RMW (Figs. 4a,b, 4e,f, and 5f), which implies a large radial gradient of Eddy_H.

In the upper boundary layer and lower troposphere, consistent with the above analyses (Fig. 5), the results change a lot, especially for the mean advection terms (Figs. 6b, d), compared to that in the lower boundary layer (Figs. 6a, c). First, the sign of mean horizontal (vertical) advection term to the TC intensification changes (Fig. 6b). Second, the mean horizontal (vertical) advective forcing changes to dominate the expansion (contraction) of the RMW from the later rapid contraction stage (Fig. 6d). As a result, the increase of the mean horizontal advective forcing (S15_ADV_H) prevents further contraction of the RMW in this layer. Note that the S15_ADV_H also contributes to the RMW contraction during the early rapid contraction stage around 17 h (Fig. 6d). In addition, both the vertical mixing forcing and eddy horizontal advective forcing play a marginal role in the RMW tendency in this layer, and the eddy vertical advective forcing changes to favor the RMW contraction.

Based on the above analyses, in addition to the curvature of the azimuthal mean tangential wind, the increase in the radial gradient of eddy horizontal advection at the RMW also plays an important role in preventing further contraction of the RMW, especially in the lower boundary layer (Fig. 6c). Since the eddy horizontal advection reflects the horizontal mixing by the resolved eddies in three-dimensions, we thus can consider that the radial gradient of (both resolved and parameterized) horizontal mixing contributes to the cessation of the RMW contraction. Note that the resolved eddy mixing in three-dimensions is implicitly parameterized by horizontal diffusion in axisymmetric simulations (Bryan and Fritsch 2002). Therefore, if the horizontal eddy mixing in three-dimensional simulation is really important for the cessation of RMW contraction, the subgrid-scale horizontal mixing in axisymmetric simulations should be important for the cessation of the RMW contraction. This may imply that larger horizontal diffusion (e.g., with a larger horizontal mixing length) in axisymmetric simulations may result in a larger steady-state RMW. This is indeed the case already given by Bryan (2012) and Rotunno and Bryan (2012). To further verify this implication, an axisymmetric model was used to perform several sensitivity experiments in the next section.

4. Axisymmetric dynamics of the RMW contraction

This section gives insights into the axisymmetric dynamics of the RMW contraction with the focus on examining the role of horizontal mixing processes in preventing the RMW contraction as implied from the three-dimensional simulations discussed in section 3.

a. Model and experimental design

The axisymmetric model selected for our numerical experiments is the state-of-the-art cloud model CM1, version 19.4 (Bryan and Fritsch 2002), which has been used widely for understanding TC dynamics (e.g., Bryan 2012; Rotunno and Bryan 2012; Bu et al. 2017). The model resolution was 3 km within a radius of 300 km and then stretched to 13 km near the lateral boundary of the model domain at 1500 km. The model had 59 vertical levels with a stretching vertical grid spacing from 25 m at the surface to 500 m at 5.5 km and remains at 500 m above. The initial TC vortex was axisymmetric with the maximum tangential wind of about 15 m s^{-1} at an 82.5-km radius, which decreases to zero with radius out to 412.5 km and the height up to 20 km. An idealized saturated and neutral sounding (Bryan and Rotunno2009) with a fixed sea surface temperature of 28 ^{o}C was used to initialize the unperturbed atmospheric environment in all simulations. The Coriolis parameter was set to 5×10^{-5} s^{-1}, corresponding to 20^{o} N. Similar to Bryan (2012), the Morrison double moment scheme was used for cloud microphysics (Morrison et al. 2009) and no cumulus convective parameterization was used. The Newtonian cooling capped at 2 K day^{-1} was used to represent longwave radiation. The ratio of surface exchange coefficients for enthalpy and momentum, C_K/C_D, was fixed at 0.5 with the C_D fixed at 2.4×10^{-3}. Following Bryan (2012), the Smagorinsky scheme (Bryan and Fritsch, 2002) was used to parameterize eddy mixings. Namely, the horizontal viscosity, $K_{m,h}$, is calculated by $K_{m,h} = l_h^2 S_h$, and the vertical viscosity, $K_{m,v}$, is calculated by $K_{m,v} = l_v^2 S_v (1 - Ri/Pr)^{1/2}$, where S_h and S_v denote horizontal and vertical deformations; Ri and Pr denote Richardson number and Prandtl number; l_h and l_v denote horizontal and vertical mixing lengths. The vertical mixing length at each level is determined by $l_v^{-2} = (kz)^{-2} + l_\infty^{-2}$, where k denotes Karman constant and l_∞ denotes asymptotic $(z \to \infty)$ vertical mixing length. In the control experiment, the l_h and l_∞ were set at 1000 m and 50 m, respectively. In addition to the control experiment, four sensitivity experiments were conducted with the l_h and l_∞ doubled and halved, respectively, during contraction period after the initial adjustment to examine the effects of horizontal and vertical mixing on the RMW contraction. Similar to the WRF simulation, every 10-min model output of CM1 were used in the analysis.

b. Results

The temporal evolution of the maximum wind speed and RMW at the lowest model level (25 m) and 250 m in the control simulation are shown in Figs. 7a and 7b. The RMW experienced an overall contraction but with large fluctuations in the early stage of simulations. Similar to that in the three-dimensional WRF simulation, the contraction stopped at the early stage of intensification by about 60 h of simulation, but the TC intensity reached a quasi-steady state after about 140 h. Note that because the initial vortex was weaker with larger RMW than that in the WRF simulation, the TC vortex experienced a longer initial adjustment period up to 48 h during which the RMW changed more irregularly and discontinuously. Since Eq. (9) assumes a continuous change of the RMW, following the current location of the RMW to predict its radial movement, we focus on the period of a nearly continuous RMW contraction after the initial adjustment or from the later rapid contraction stage (i.e., 48 h). Similar to the analysis in section 3, the model output after the initial 48 h of simulation was also filtered and interpolated onto a 50-m radial resolution. As expected, the method of S15 and W82 can capture the RMW tendency very well in the axisymmetric simulation (Fig. 7c).

To understand the dynamics of the RMW contraction, a tangential wind budget during the contraction period (50 h) was conducted as what was done in section 3c. All the tangential wind tendency terms in Eq. (10) excepted for those eddy terms were direct output from the model simulation. Note that these tendencies were not averaged in time because the budgeted tendency at any given time (e.g., Fig. 8b) can well capture the tendency from the model (e.g., Fig. 8a). Overall, the results are consistent with those from the WRF model simulations. The local tendency of tangential wind is larger inside the RMW than outside during the contraction period, corresponding to the RMW contraction (Fig. 7). Contributions by (both horizontal and vertical) advection terms varies with height (Figs. 8c–d). The direct contribution by vertical mixing (and surface fiction) makes the RMW expansion in the boundary layer (Fig. 8e). As expected, the horizontal mixing in the boundary layer is larger than that in the WRF simulation and contributes to the RMW expansion (Fig. 8f), similar to the eddy horizontal advection in the WRF simulations.

The individual tendencies in Eq. (10) at the RMW below and above 500-m height and their corresponding contributions to the RMW tendency in Eq. (11) are shown in Fig. 9. The overall results are consistent with those from the WRF model simulations. First, except for the horizontal advection (ADV_H), all other terms slow down the TC intensification rate during the intensification period in the lower boundary layer (Fig. 9a), and the sign of mean horizontal (vertical) term to the TC intensification changes from the lower boundary layer (Fig. 9a) to the upper boundary layer and lower troposphere (Fig. 9b). Second, the horizontal advective forcing (S15_ADV_H) dominantly contributes to the RMW contraction in the lower boundary layer (Fig. 9c) but expansion above (Fig. 9d). In addition, the vertical advective forcing on RMW tendency (S15_ADV_V) is mainly positive during the rapid contraction period (48–57 h) and plays a small role later in the lower boundary layer (Fig. 9c), but dominantly contributes to the RMW contraction throughout the analysis period in the upper boundary layer and lower troposphere (Fig. 9d). As expected, the horizontal mixing forcing (S15_Diff) increases during the rapid contraction period, and then makes an obvious inhibitory effect on the RMW contraction in the lower boundary layer (Fig. 9c), similar to the resolved eddy horizontal advection/mixing shown in Fig. 6c in the three-dimensional WRF simulation. Note that Diff and S15_Diff in Fig. 6 are different from those in Fig. 9, in which both the resolved and parameterized horizontal mixing are included as mentioned above. In addition, turbulent vertical mixing including surface friction (Ff) also contributes to the cessation of the RMW contraction in the lower boundary layer (Fig. 9c). Note that although the Ff in the contraction stage is about twice the value of Diff in the lower boundary layer (Fig. 9a), their contributions (S15_Ff and S15_Diff) to the RMW tendency are comparable with each other (Fig. 9c) because the contours of Diff are more parallel to the RMW than that of Ff (cf. Fig. 8e, f), consistent with the analysis in the three-dimensional WRF simulation. In addition, the roles of Ff and S15_Diff become marginal above the lower boundary layer (Fig. 9d).

The above analyses for the control axisymmetric simulation demonstrate that horizontal advective forcing predominantly contributes to the RMW contraction during the RMW contraction period in the lower boundary layer, while the horizontal mixing forcing plays an important role in preventing the RMW contraction, as the eddy horizontal advection in three-dimensional simulations. In addition, the vertical mixing (including surface friction) forcing also plays an important role in the cessation of RMW contraction. These two conclusions are further confirmed by results from four sensitivity experiments, in which the horizontal mixing length and the asymptotic vertical mixing length were doubled or halved of that used in the control experiment from 48 h of simulation in the control experiment. Figure 10 shows the evolutions of the RMW (Figs. 10a, c) and the corresponding mixing forcing (S15_Diff, S15_Ff; Figs. 10b, d). As expected, the increased horizontal and vertical mixing slowed down the RMW contraction in the rapid RMW contraction period (Figs. 10b and 10d) and resulted in a larger steady-state RMW (Figs. 10a and 10c), which are consistent well with Bryan (2012) and Bu et al. (2017). Therefore, our results indicate that in addition to the sharpness of tangential wind as identified by S15, eddy and/or subgrid-scale mixing also play an important role in slowing down and finally stopping the RMW contraction in TCs.

5. Concluding remarks

In this study, we have revisited the dynamics of the RMW contraction in TCs based on both theoretical consideration and diagnostics of high-resolution axisymmetric and three-dimensional numerical simulations. The existing theories are first reviewed and evaluated using idealized numerical simulation results. Dynamically, the RMW contraction results from larger tangential wind tendency inside of the RMW than that outside of it. The balanced response of a TC vortex to eyewall heating, which shows a larger tangential wind tendency inside the RMW, is considered to be the major reason for TC eyewall contraction (Shapiro and Willoughby 1982). This concept was quantified based on the definition of the directional derivative in a moving frame of reference following the RMW of a TC (W82).

More recently, K12 and S15 developed different frameworks for RMV contraction. Although the equation of K12 could be simplified to the RMW tendency equation of W82 under some assumptions, the framework of S15 can provide a tendency equation of the RMW without any assumption/simplification. We have shown that both W82 and S15 can reproduce precisely the changing rate of RMW in idealized high-resolution numerical simulations in both three-dimensional and axisymmetric models. However, compared with that of W82, an extension of equation of S15 can be further used to provide insights into the dynamics of the RMW contraction. Based on S15, the rate of the RMW change is directly proportional to the radial gradient of local tangential wind and inversely proportional to the curvature or sharpness of tangential wind at the RMW. In addition to the increase of the sharpness, as suggested by S15, this study indicates that the decrease in the negative radial gradient of azimuthal mean tangential wind tendency also contributes to the cessation of the RMW contraction.

The azimuthal-mean tangential wind budget, based on the three-dimensional and axisymmetric idealized simulations, indicates that the mean horizontal advective forcing contributes predominantly to the RMW contraction (expansion) in the lower boundary layer (the upper boundary layer and lower troposphere) in the later rapid contraction stage. The mean vertical advective forcing is secondary but also plays a role in the lower boundary layer, particularly during the rapid contraction stage, but contributes predominantly to the RMW contraction above. Overall, the vertical mixing and surface friction often lead to the RMW expansion and the cessation of RMW mainly in the lower boundary layer. An interesting finding is that in addition to the increase of sharpness of tangential wind, with the TC intensification, the increase of radial gradient of (both resolved and parameterized) horizontal mixing also slows down the RMW contraction, mainly in the lower boundary layer, and subsequently contributes to the cessation of the RMW contraction. Note that although the conclusions here are similar to those in K12, Kieu and Zhang (2017), and Qin et al. (2018), in which the mean advection effects make a net positive while the mixing effects make a net negative impact on the RMW contraction, we refer to the radial gradient of these processes while K12 and KZ17 referred to those processes themselves.

Finally, note that the framework of S15 assume continuous changes of the RMW in both time and space. As a result, the method can not be applied to understand discontinuity or jump of the RMW, such as prior to the formation of an eyewall structure and the concentric eyewall replacement. Note that in the diagnostic viewpoint W82 is still valid even the RMW change is discontinuous because the directional derivative is involved. In addition, although the resolved eddy mixing prevents the RMW contraction, it may contribute positively to the initial organization of the eyewall through the eddy-mean flow interaction. Therefore, eddy processes could play different roles in different stages of a TC. This remains an issue for a future study.

Acknowledgments: The authors thank three anonymous reviewers for their thoughtful review comments. This study has been supported in part by National Natural Science Foundation of China under grant 41730960 and in part by NSF grants AGS-1326524 and AGS-1834300. Y. Li is funded by China Scholarship Council (File 201806210324).

References

Bryan, G. H., and J. M. Fritsch, 2002: A benchmark simulation for moist nonhydrostatic numerical model. *Mon. Wea. Rev.*, **130**, 2917-2928, doi:10.1175/1520-0493(2002)130<2917:ABSFMN>2.0.CO;2.

Bryan, G.H., and R. Rotunno, 2009: Evaluation of an analytical model for the maximum intensity of tropical cyclones. *J. Atmos. Sci.,* **66**, 3042–3060, doi:10.1175/2009JAS3038.1.

Bryan, G. H., 2012: Effects of surface exchange coefficients and turbulence length scales on the intensity and structure of numerically simulated hurricanes. *Mon. Wea. Rev.,* **140**, 1125–1143, doi:10.1175/MWR-D-11-00231.1.

Bryan, G. H., 2013: Comments on 'Sensitivity of tropical-cyclone models to the surface drag coefficient'. *Q. J. R. Meteorol. Soc.*, **139**, 1957-1960, doi:10.1002/qj.2066.

Bu, Y. P., R. G. Fovell, and K. L. Corbosiero, 2017: The influences of boundary layer mixing and cloud-radiative forcing on tropical cyclone size. *J. Atmos. Sci.,* **74**, 1273–1292, doi:10.1175/JAS-D-16-0231.1.

Bui, H. H., R. K. Smith, M. T. Montgomery, J. Peng, 2009: Balanced and unbalanced aspects of tropical cyclone intensification. *Quart. J. Roy. Meteor. Soc.*, **135**, 1715-1731, doi:10.1002/qj.502.

Deng, L., T. Li, M. Bi, J. Liu, M. Peng, 2018: Dependence of tropical cyclone development on Coriolis parameter: A theoretical model. *Dyn. Atmos. Ocean*, 81, 51-62, doi:10.1016/j.dynatmoce.2017.12.001.

Dudhia, J., 1989: Numerical study of convection observed during the winter monsoon experiment using a mesoscale two-dimensional model. *J. Atmos. Sci.*, **46**, 3077-3107, doi:10.1175/1520-0469(1989)046<3077:NSOCOD>2.0.CO;2.

Dunion, J.P. and C.S. Marron, 2008: A reexamination of the Jordan mean tropical sounding based on awareness of the Saharan air layer: Results from 2002. *J. Climate,* **21**, 5242–5253, doi:10.1175/2008JCLI1868.1.

Eliassen, A., 1951: Slow thermally of frictionally controlled meridional circulation in a circular vortex. *Astrophys. Norv.*, **5**, 19-60.

Fudeyasu, H. and Y. Wang, 2011: Balanced contribution to the intensification of a tropical cyclone simulated in TCM4: Outer-core spinup process. *J. Atmos. Sci.,* **68**,430–449, doi:10.1175/2010JAS3523.1.

Heng, J. and Y. Wang, 2016: Nonlinear response of a tropical cyclone vortex to prescribed eyewall heating with and without surface friction in TCM4: Implications for tropical cyclone intensification. *J. Atmos. Sci.,* **73**, 1315–1333, doi:10.1175/JAS-D-15-0164.1.

Heng, J., Y. Wang, and W. Zhou, 2017: Revisiting the balanced and unbalanced aspects of tropical intensification. *J. Atmos. Sci*., **74**, 2575-2591, doi:10.1175/JAS-D-17-0046.1.

Kain, J. S. 2004: The Kain–Fritsch convective parameterization: an update. *J. Appl. Meteor*., **43**, 170-181, doi:10.1175/1520-0450(2004)043<0170:TKCPAU>2.0.CO;2.

Kieu, C. Q., 2012: An investigation into the contraction of the hurricane radius of maximum wind. *Meteorol. Atmos. Phys.*, **115**, 47-56, doi:10.1007/s00703-011-0171-7.

Kieu, C. Q., and D.-L. Zhang, 2017: Comments on “Revisiting the relationship between eyewall contraction and intensification”. *J. Atmos. Sci.,* **74**, 4265–4274, doi:10.1175/JAS-D-17-0011.1.

Kilroy, G., M. T. Montgomery, and R. K. Smith, 2017: The role of boundary-layer friction on tropical cyclogenesis and subsequent intensification. *Q. J. R. Meteorol. Soc.*, **143**, 2524-2536, doi:10.1002/qj.3104.

Mlawer, E. J., S. J. Taubman, P. D. Brown, M. J. Iacono, and S. A. Clough, 1997: Radiative transfer for inhomogeneous atmospheres: RRTM, a validated correlated-k model for the longwave. *J. Geophys. Res.*, **102**, 16663-16682, doi:10.1029/97JD00237.

Morrison, H., G. Thompson, and V. Tatarskii, 2009: Impact of cloud microphysics on the development of trailing stratiform precipitation in a simulated squall line: Comparison of one- and two- moment scheme. *Mon. Wea. Rev.*, 137, 991-1007, doi:10.1175/2008MWR2556.1.

Nakanishi, M., and H. Niino, 2009: Development of an improved turbulence closure model for the atmospheric boundary layer. *J. Meteorol. Soc. Japan*, **87**, 895-912, doi:10.2151/jmsj.87.895.

Pendergrass, A.G. and H.E. Willoughby, 2009: Diabatically induced secondary flows in tropical cyclones. Part I: Quasi-steady forcing. *Mon. Wea. Rev.,* **137**, 805–821, doi:10.1175/2008MWR2657.1.

Qin, N., D.-L. Zhang, and Y. Li, 2016: A statistical analysis of steady eyewall sizes associated with rapidly intensifying hurricanes. *Wea. Forecasting,* **31**, 737–742, doi:10.1175/WAF-D-16-0016.1.

Qin, N., D.-L. Zhang, W. Miller, and C. Q. Kieu, 2018: On the rapid intensification of Hurricane Wilma (2005). Part IV: Inner-core dynamics during the steady radius of maximum wind stage. *Q. J. R. Meteorol. Soc.*, **144**, 2508-2523, doi:10.1002/qj.3339.

Rotunno, R. and G. H. Bryan, 2012: Effects of parameterized diffusion on simulated hurricanes. *J. Atmos. Sci.,* **69**, 2284–2299, doi:10.1175/JAS-D-11-0204.1.

Schubert, W. H. and J. J. Hack, 1982: Inertial stability and tropical cyclone development. *J. Atmos. Sci.,* **39**, 1687–1697, doi:10.1175/1520-0469(1982)039%3C1687:ISATCD%3E2.0.CO;2.

Shapiro, L. J. and H. E. Willoughby, 1982: The response of balanced hurricanes to local sources of heat and momentum. *J. Atmos. Sci.,* **39**, 378–394, doi:10.1175/1520-

0469(1982)039%3C0378:TROBHT%3E2.0.CO;2.

Skamarock, W. C., J. B. Klemp, J. Dudhia, D. O. Gill, D. M. Barker, W. Wang, and J. G. Powers, 2008: A description of the Advanced Research WRF version 3. *NCAR Tech Note-4751STR*, 113 pp, doi:10.5065/D68S4MVH.

Smith, R. K., G. Kilroy, and M. T. Montgomery, 2015: Why do model tropical cyclones intensify more rapidly at low latitudes? *J. Atmos. Sci.,* **72**, 1783–1804, doi:10.1175/JAS-D-14-0044.1.

Smith, R. K., M. T. Montgomery, and G. L. Thomsen, 2014: Sensitivity of tropical-cyclone models to the surface drag coefficient in different boundary-layer schemes, *Q. J. R. Meteorol. Soc.*, **140**, 792-804, doi:10.1002/qj.2057.

Stern, D. P., J. L. Vigh, D. S. Nolan, and F. Zhang, 2015: Revisiting the relationship between eyewall contraction and intensification. *J. Atmos. Sci.,* **72**, 1283–1306, doi:10.1175/JAS-D-14-0261.1.

Stern, D. P., J. L. Vigh, D. S. Nolan, and F. Zhang, 2017: Reply to "Comments on 'Revisiting the relationship between eyewall contraction and intensification.'" *J. Atmos. Sci.,* **72**, 4275–4286, doi:10.1175/JAS-D-17-0120.1.

Tang, X., Z. Tan, J. Fang, E.B. Munsell, and F. Zhang, 2019: Impact of the diurnal radiation contrast on the contraction of radius of maximum wind during intensification of Hurricane Edouard (2014). *J. Atmos. Sci.,* **76**, 421–432, doi:10.1175/JAS-D-18-0131.1.

Thompson, G., P.R. Field, R.M. Rasmussen, and W.D. Hall, 2008: Explicit forecasts of winter precipitation using an improved bulk microphysics scheme. Part II: Implementation of a new snow parameterization. *Mon. Wea. Rev.*, **136**, 5095-5115, doi:10.1175/2008MWR2387.1.

Wang, H., C. Wu, and Y. Wang, 2016: Secondary eyewall formation in an idealized tropical cyclone simulation: Balanced and unbalanced dynamics. *J. Atmos. Sci.,* **73**,3911–3930, doi:10.1175/JAS-D-15-0146.1.

Wang, Y. and H. Wang, 2013: The inner-core size increase of Typhoon Megi (2010) during its rapid intensification phase. *Tropical Cyclone Res. Rev.*, **2**, 65-80, doi:10.6057/2013TCRR02.01.

Wang, Y. and J. Xu, 2010: Energy production, frictional dissipation, and maximum intensity of a numerically simulated tropical cyclone. *J. Atmos. Sci.,* **67**, 97–116, doi:10.1175/2009JAS3143.1.

Willoughby, H. E., J. A. Clos, and M. G. Shoreibah, 1982: Concentric eye walls, secondary wind maxima, and the evolution of the hurricane vortex. *J. Atmos. Sci.,* **39**, 395–411, doi:10.1175/1520-0469(1982)039<0395:CEWSWM>2.0.CO;2.

Willoughby, H.E., 1990: Temporal changes of the primary circulation in tropical cyclones. *J. Atmos. Sci.,* **47**, 242–264, doi:10.1175/1520-0469(1990)047<0242:TCOTPC>2.0.CO;2.

Xu, J. and Y. Wang, 2010a: Sensitivity of tropical cyclone inner-core size and intensity to the radial distribution of surface entropy flux. *J. Atmos. Sci.,* **67**, 1831–1852, doi: 10.1175/2010JAS3387.1.

Xu, J. and Y. Wang, 2010b: Sensitivity of the simulated tropical cyclone inner-core size to the initial vortex size. *Mon. Wea. Rev.,* **138**, 4135–4157, doi:10.1175/2010MWR3335.1.

Zhu, Z., and P. Zhu, 2014: The role of outer rainband convection in governing the eyewall replacement cycle in numerical simulations of tropical cyclones. *J. Geophys. Res. Atmos*., **119**, 8049-8072, doi:10.1002/2014JD021899.

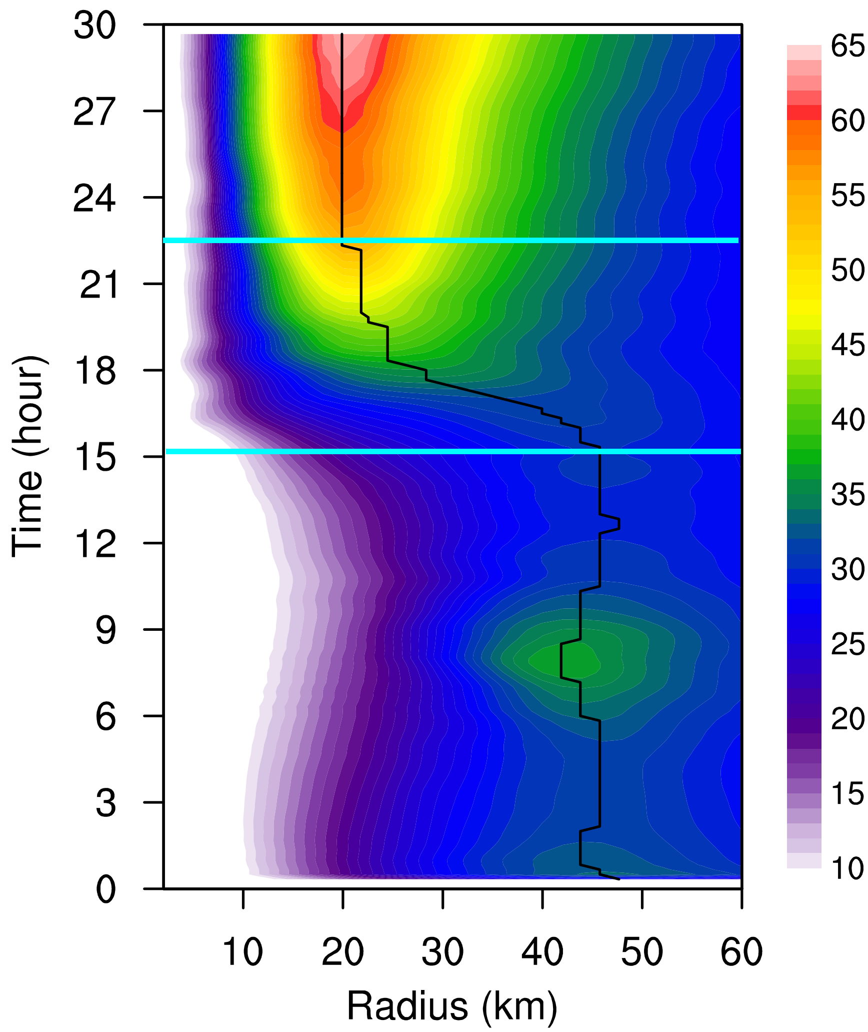

FIG. 1. Radius–time Hovmöller plot of the azimuthal mean tangential wind speed (shades, m s^{-1}) at a height of 250 m, overlaid by the radial position of RMW (black), and the two cyan horizontal lines mark the rapid contraction period of the RMW.

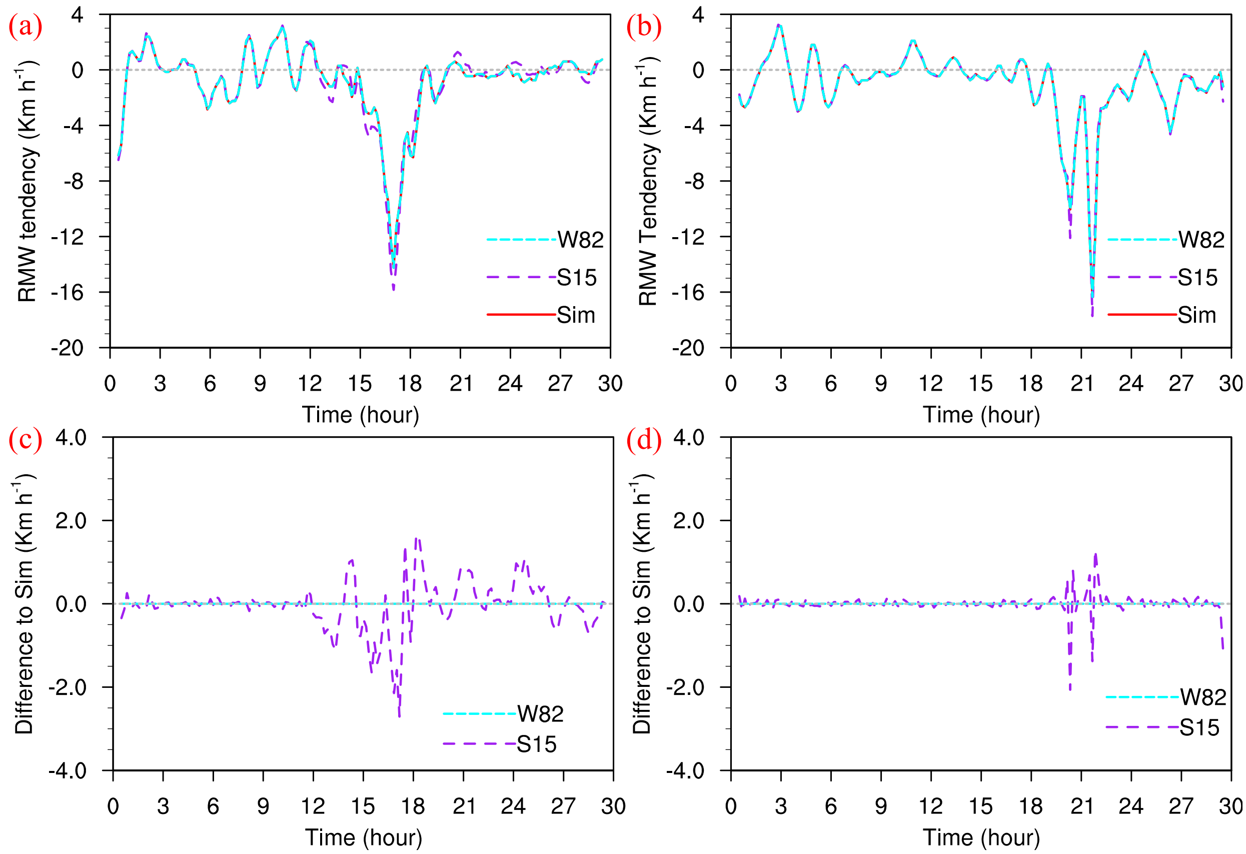

FIG. 2. (a) Time series of the tendency of the RMW simulated in control experiment (red solid) and diagnosed by S15 (purple dashed) and W82 (cyan dashed), respectively. (b) Same as (a), but for the sensitivity experiment with an initially weak TC vortex of maximum wind speed of 18 m s^{-1}. (c)–(d) Same as (a)–(b), but showing the difference between the diagnosed and simulated results.

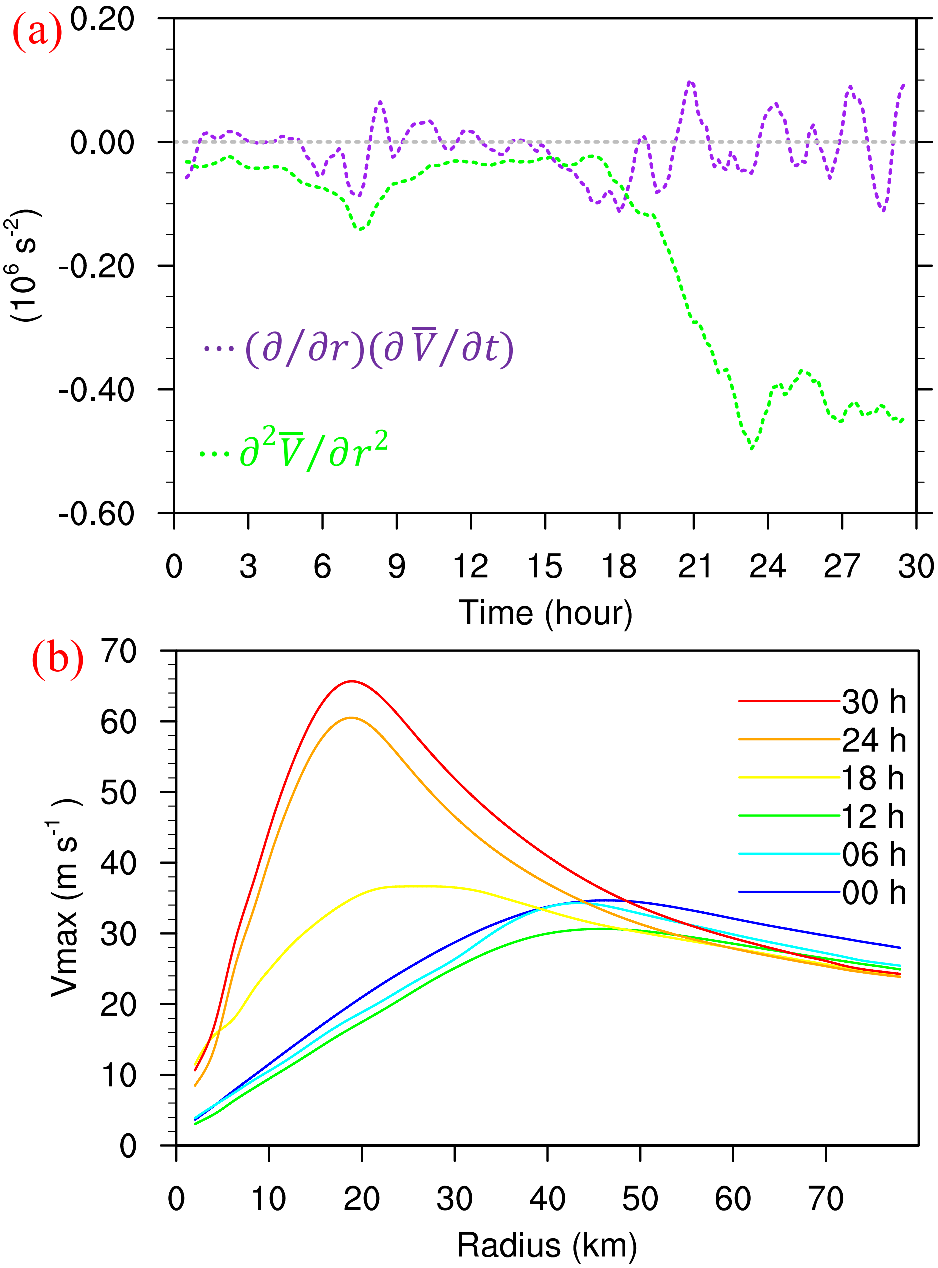

FIG. 3. (a) Time series of the radial gradient of time tendency of the azimuthal mean tangential wind [$(\partial/\partial r)(\partial\overline{V}/\partial t)$; purple dashed] and the curvature of the azimuthal mean tangential wind in radial direction at the RMW ($\partial^2 V/\partial r^2$; green dotted) at a height of 250 m. (b) The radial profile of the azimuthal mean tangential wind speed at a height of 250 m.

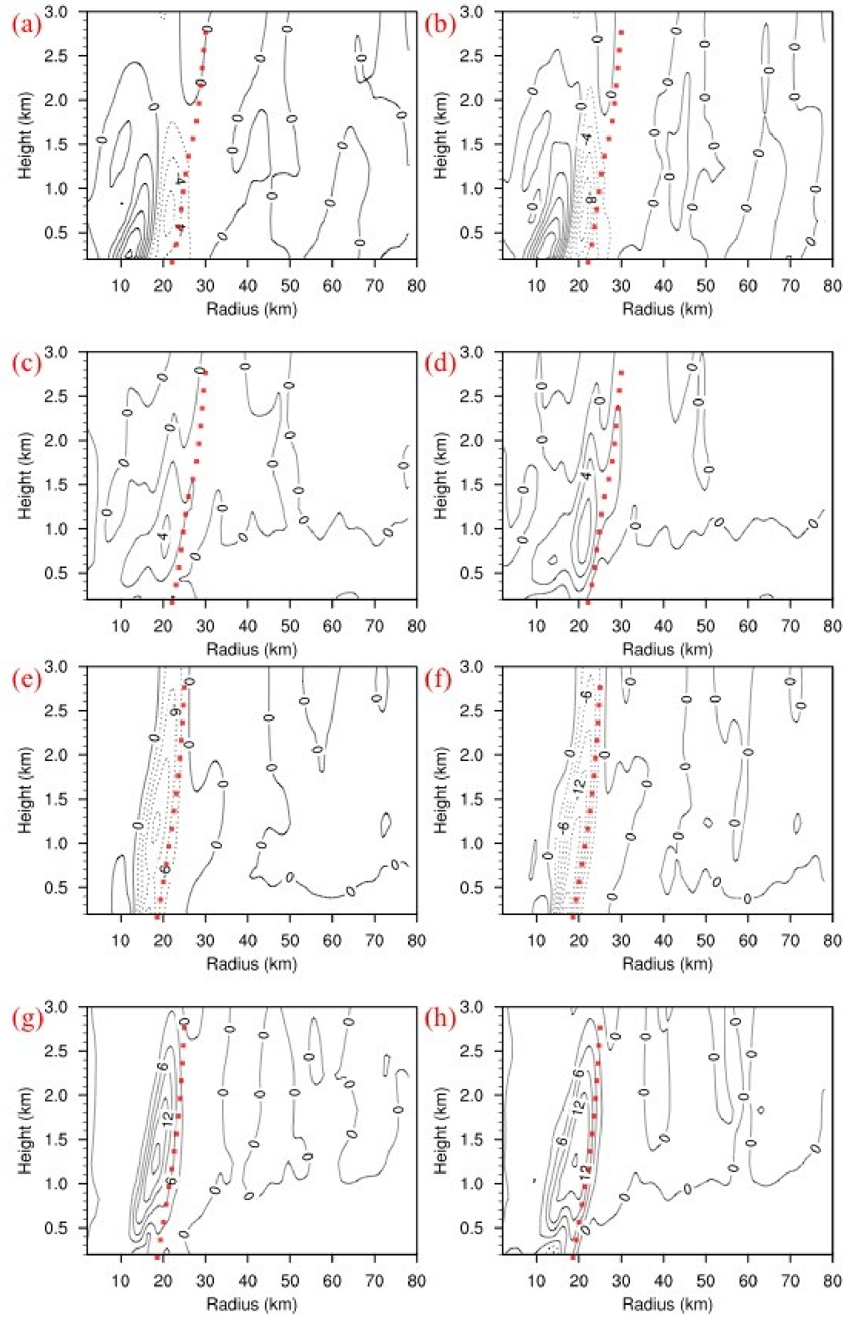

FIG. 4. Radius–height cross-sections of the (a)–(b) eddy horizontal advection at 19 h with an 40-min average, from (a) direct off-line calulation based on 10-min average wind field and (b) average between the direct off-line calculation and the difference between total horizontal advection and the off-line calculated mean horizontal advection. (c)–(d) Same as (a)–(b), but for vertical advection. The contour interval is 2 m s^{-1} h^{-1}. (e)–(h) Same as (a)–(d), but for 21 h with an contour interval of 3 m s^{-1} h^{-1}.

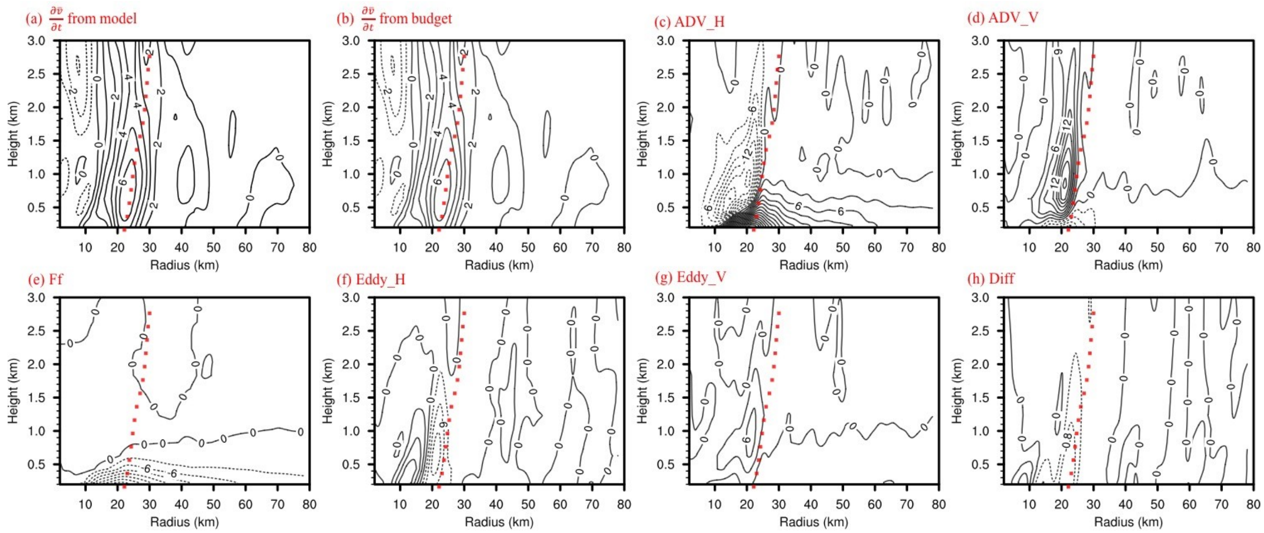

FIG. 5. Radius–height cross-sections of the averaged local accelaration of the azimuthal mean tangential wind at 19 h with a 40-min average of simulaiton based on (a) model simulaiton and (b) budget. (c)–(h) Same as (b), but for the individual contributions by mean horizontal advection, mean vertical advection, vertical mixing including surface friction, eddy horizontal advection, eddy vertical advection, and horizontal diffusion terms, respectively. The contour interval is 1 m s^{-1} h^{-1} in (a)–(b); 3 m s^{-1} h^{-1} in (c)–(g); and 0.4 m s^{-1} h^{-1} in (h). The red dotted line shows the RMWs at different vertical levels.

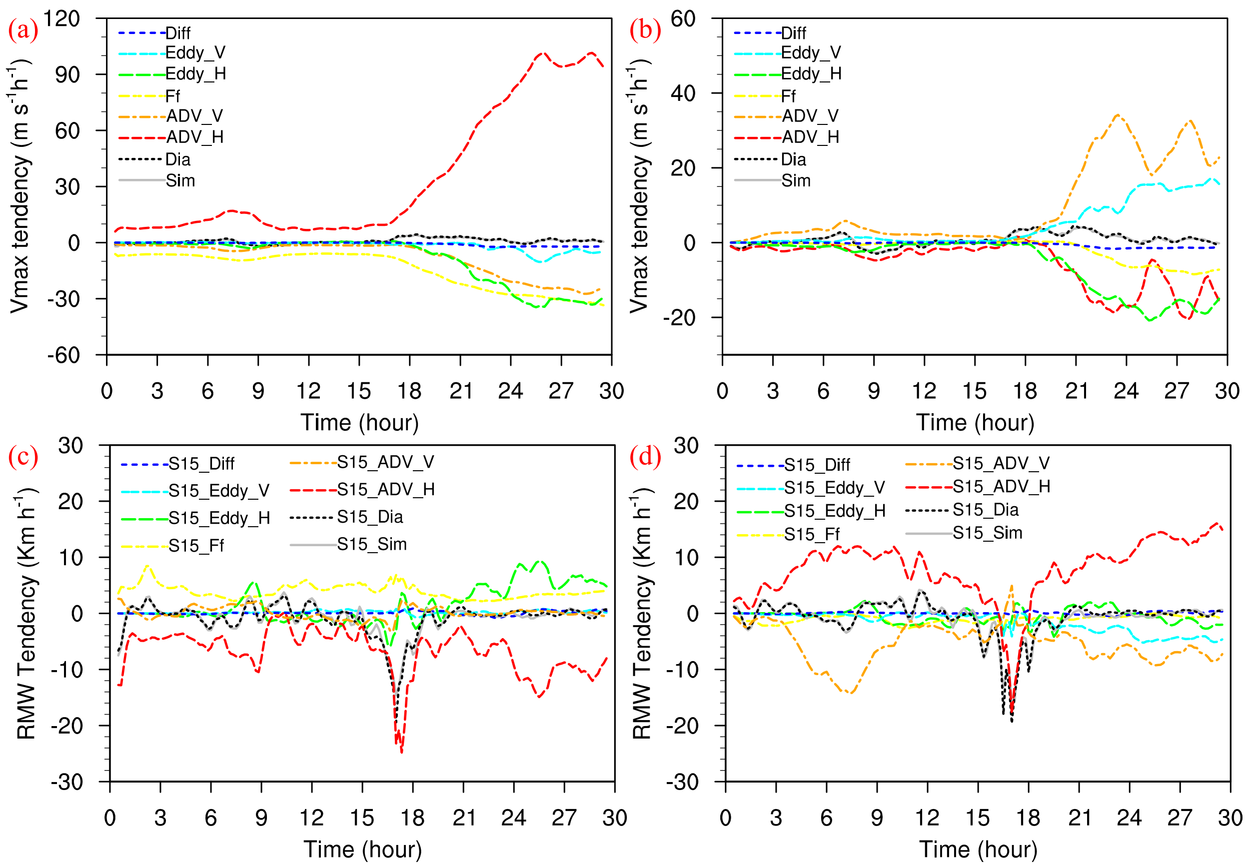

FIG. 6. (a) Time series of each tangential wind tendency at the RMW averaged below 500-m height. (b) Same as (a), but averaged between 500–1500-m height. (c)–(d) Same as (a)–(b), but for the contributions by each tangential wind tendency to the RMW tendency.

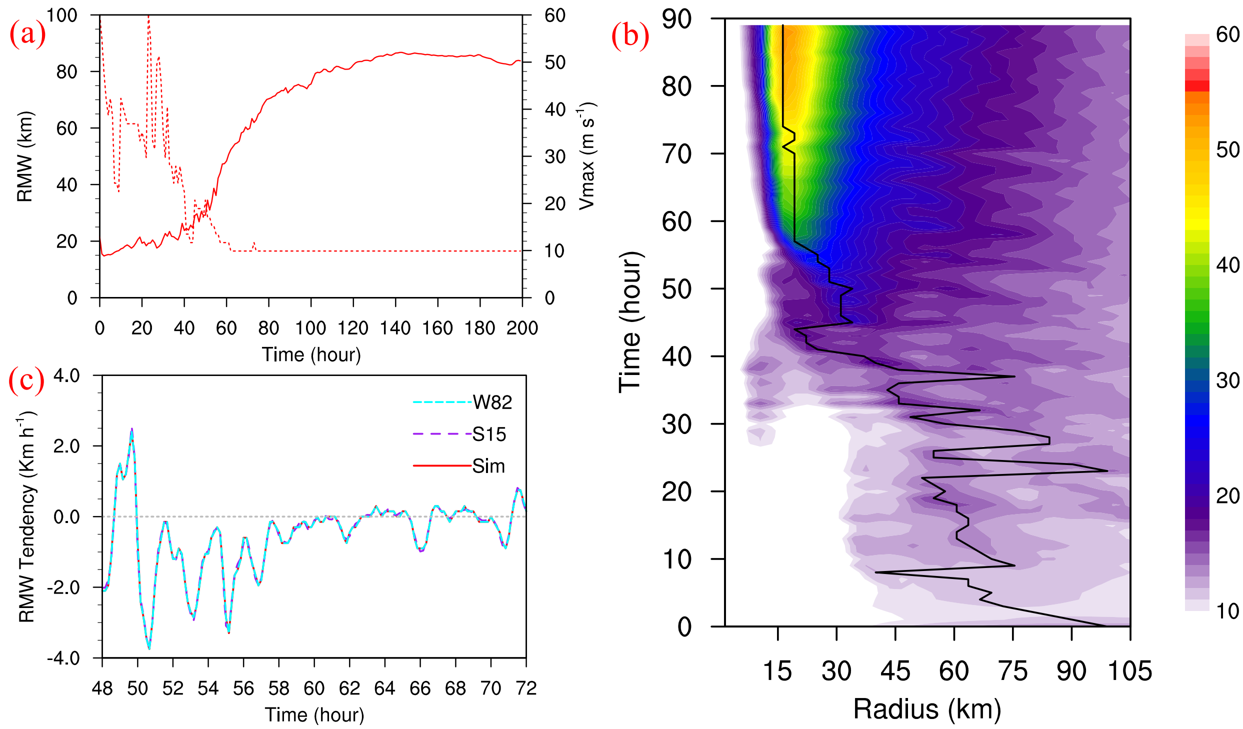

FIG. 7. (a) Time series of the maximum azimuthal-mean tangential wind speed (Vmax; red solid) at the lowest model level (25 m) and its corresponding radius (RMW; red dotted). (b) and (c) Same as Fig. 1 and Fig. 2, but for the control experiment from CM1.

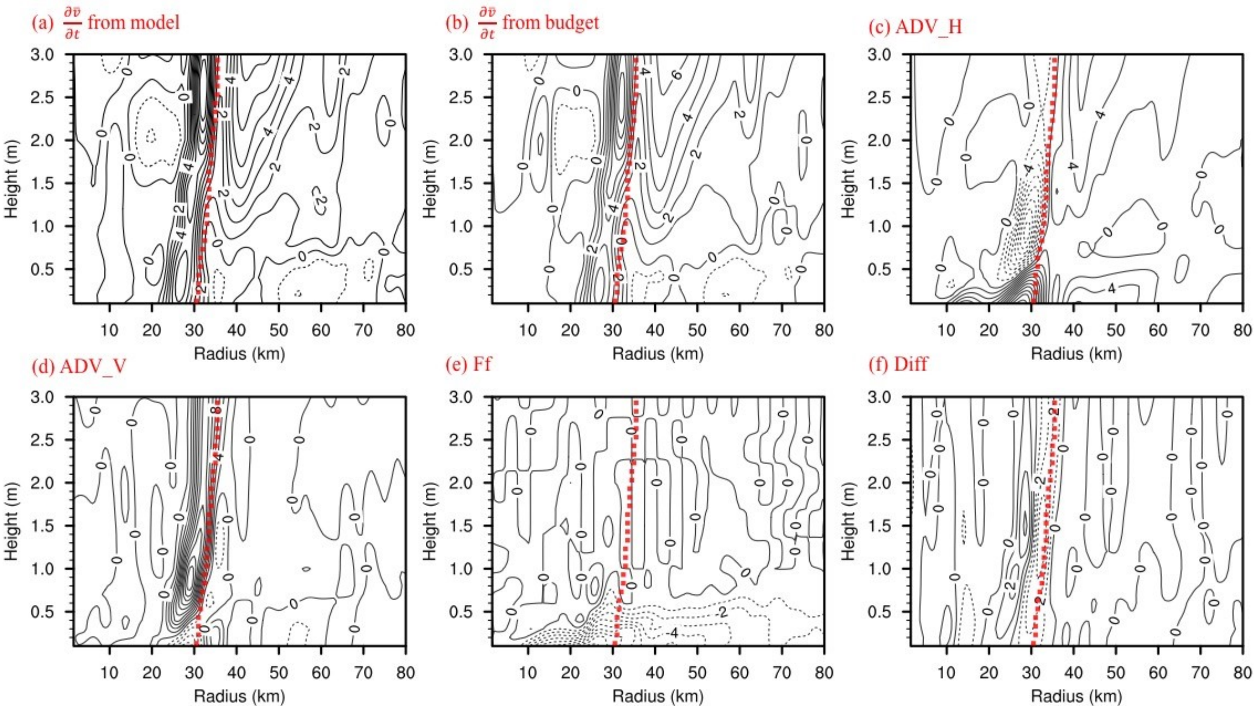

FIG. 8. Same as Fig. 5, but for the control experiment from CM1 at 50 h with a 40-min average, and the eddy terms are excluded here. The contour interval is 1 m s^{-1} h^{-1} in (a)–(b) and (e)–(f); and 2 m s^{-1} in (c)–(d).

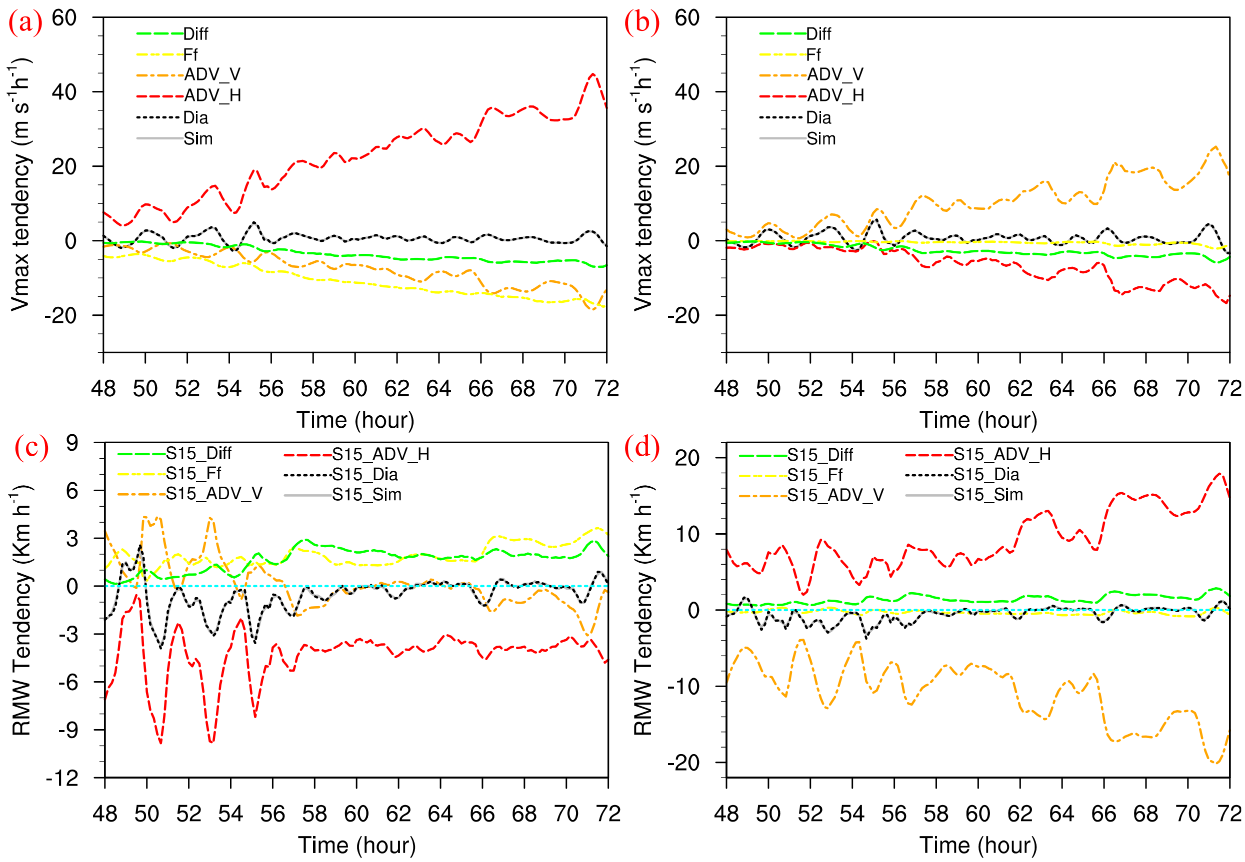

FIG. 9. Same as Fig. 6, but for the control experiment from CM1 with the eddy terms being excluded.

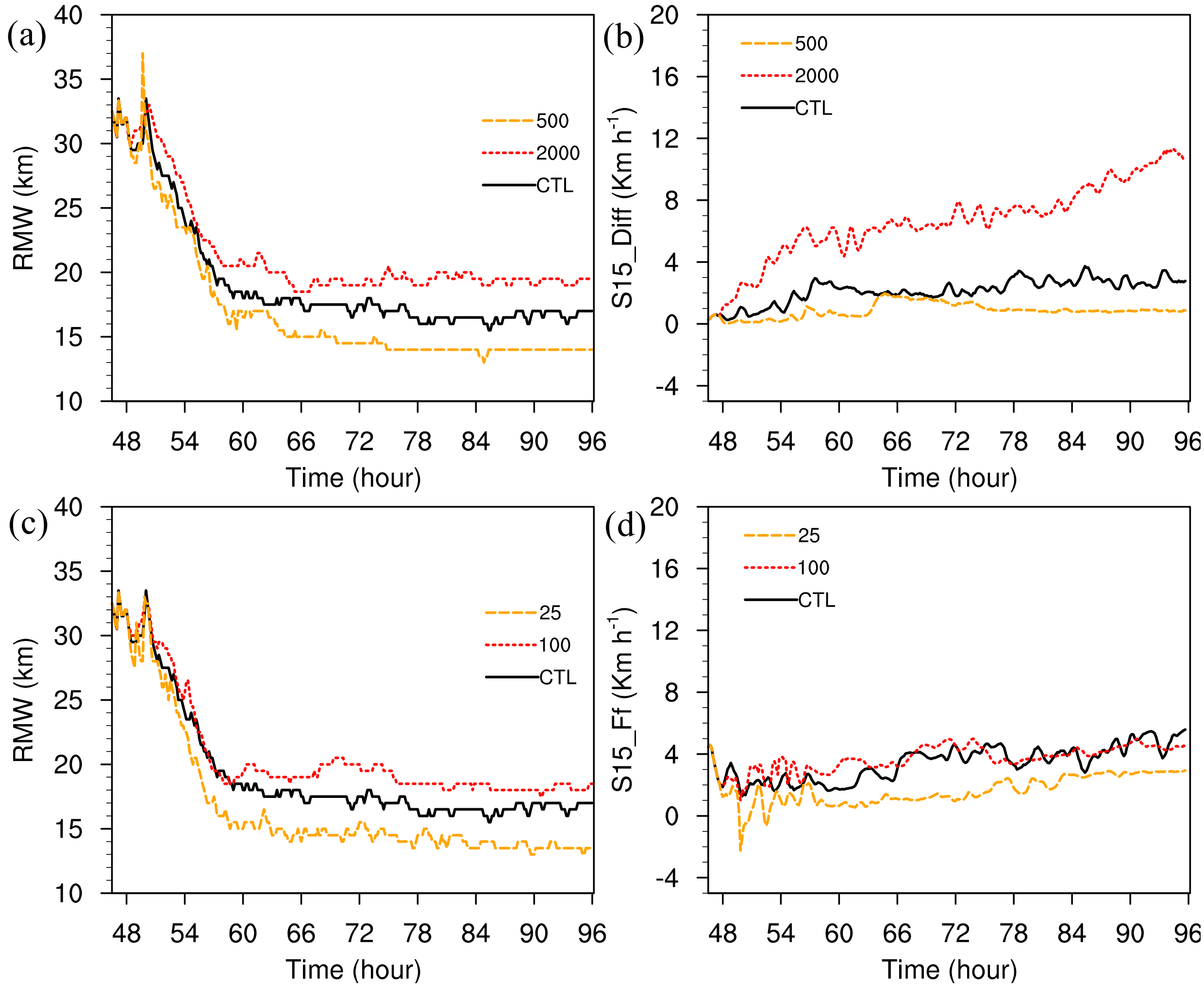

FIG. 10. (a) Time series of RMW at 250 m from CM1 for control experiment (CTL; black solid), and sensitivity experiments with the horizontal mixing length doubled (2000; red dotted) and halved (500; yellow dashed). (b) Same as (a), but showing S15_Diff. (c) Same as (a), but with the asymptotic vertical mixing length doubled (100; red dotted) and halved (25; yellow dashed). (d) Same as (c), but showing S15_Ff.